Technical Note

Computational and Experimental Studies of an Orthopedic Implant: MRI-Related Heating at 1.5-T/64-MHz and 3-T/128-MHz

Yan Liu, BS,[1] Ji Chen, PhD,[1*] Frank G. Shellock, PhD,[2] and Wolfgang Kainz, PhD[3]

Purpose: To use numerical modeling to predict the worst-case of magnetic resonance imaging (MRI)-induced heating of an orthopedic implant of different sizes under 1.5-T/64-MHz and 3-T/128-MHz conditions and to apply the experimental test to validate the numerical results for worst-case heating.

Materials and Methods: Investigations of specific absorption rate (SAR) and the temperature rise of an orthopedic implant of different sizes within a standard phantom were accomplished by numerical finite-difference time-domain modeling and experimental measurements. MRI-related heating experiments were performed using standardized techniques at 1.5-T/64-MHz and 3-T/128-MHz.

Results: The numerical modeling results indicated that the induced energy deposition is almost linearly related to the dimension of the orthopedic implant when it is less than 100 mm for 1.5-T/64-MHz and 3-T/128-MHz conditions. At 3-T/128-MHz, when the dimension is greater than 100 mm, the linear relation does not exist, which suggests a wavelength effect at higher frequency. Higher temperature rises occurred at 1.5-T/64-MHz MRI than at 3-T/128-MHz for both numerical modeling and experimental studies.

Conclusion: The numerical technique predicted which device size had maximum heating and its location. Temperature rise data agreed well with thermal simulation results. The presented method proved to be suitable to assess MRI-induced heating of complex medical implants.

Key Words: MRI safety; heating; electromagnetic modeling; medical implants
J. Magn. Reson. Imaging 2012; 000:000–000.

WITH THE INCREASED USE of implantable medical devices, there have been concerns related to magnetic resonance imaging (MRI) issues including magnetic field interactions, heating, and artifacts (1). Notably, MRI-related heating is potentially dangerous for patients with implants that have an elongated shape and/or that form a closed conducting loop of a certain diameter (1). Accordingly, MRI safety issues are generally characterized for implants and devices to ensure patient safety according to recommendations from the Food and Drug Administration (FDA) that are based on those appropriate test procedures presented by the American Society for Testing and Materials (ASTM) International (3).

With regard to MRI-related heating, the ASTM International has set forth test procedures that involve placing the implant in a gelled-saline-filled phantom in a position with high and well-characterized specific absorption rate (SAR) distribution and recording temperatures at multiple sites on the implant during an MRI procedure applied using a relatively high level of radiofrequency (RF) energy, as indicated by the SAR (3). This procedure gives a conservative estimation of device heating (temperature rise) compared with actual in vivo cases due to the test placement of the device. Given the fact that many implants, especially orthopedic implants, may have complicated shapes as well as various possible dimensions depending on the clinical requirements (eg, an orthopedic implant may have different lengths available depending on the size needed for the patient), it is particularly challenging to experimentally assess MRI-related heating for each version of a given type of implant. Of further note, significant experimental effort is required to test all possible sizes and combinations of the implant and to locate the maximum heating location on the implant's surface. As such, using the ASTM heating phantom with the implant, it may be necessary to place multiple temperature probes on and around the periphery of the implant to identify the worst-case heating

[1]Department of Electrical and Computer Engineering, University of Houston, Houston, Texas, USA.
[2]Keck School of Medicine, University of Southern California and Institute for Magnetic Resonance Safety, Education, and Research, Los Angeles, California, USA.
[3]Center for Devices and Radiological Health, Food and Drug Administration, Silver Spring, Maryland, USA.

Disclaimer: The mention of commercial products, their sources or their use in connection with material reported herein is not to be construed as either an actual or implied endorsement of such products by the Department of Health and Human Services.

*Address reprint requests to: J.C., Department of Electrical and Computer Engineering, University of Houston, Houston, TX 77204. E-mail: jchen18@uh.edu

Received January 27, 2012; Accepted June 29, 2012.
DOI 10.1002/jmri.23764
View this article online at wileyonlinelibrary.com.

location. Even by following this strategy, it is not guaranteed that the maximum heating location will be found. Accordingly, the time, effort, and monetary factors needed to properly study the combinations of all these parameters experimentally can be prohibitive.

With recent advances in numerical modeling for electromagnetic fields (4,5), it is now feasible to perform rigorous simulations of implant heating exposed to MRI conditions. Therefore, rather than placing the implant inside the ASTM heating phantom and recording temperatures for each configuration and size at various locations on the implant's surface, electromagnetic simulations may be used to determine the maximum heating location for each implant size and configuration. The advantage of the numerical simulation results is that it provides the heating pattern for the entire implant surface. In addition, the surface heating pattern of various orientations relative to the incident electric field can also be obtained. With all simulation results, it is possible to identify the worst-case heating and the location of the maximum heating for the entire device family. Then, only the worst-case heating configuration at the worst-case heating location on the implant's surface needs to be experimentally verified using the technique described by the ASTM International (3). Notably, this combined modeling and experiment approach can quickly identify, in a cost-effective and timely manner, the worst-case heating for an entire implant family.

The numerical modeling approach typically begins with electromagnetic simulations to determine the SAR distribution and associated temperature rise in the vicinity of the implant in a phantom. The ASTM heating phantom (3) is used for both the experimental and computational studies. Most modeling tools have the capability to directly import engineering designs in their native CAD (computer aided design) format, which significantly simplifies the modeling procedure (4). By being able to use the original CAD data of the implant, it is possible to accurately represent the device in the computational tool. This accurate representation of the implant guarantees correct thermal heating patterns for practical medical device designs (5).

To illustrate the efficiency of this approach, the current investigation used rigorous numerical simulations to investigate the heating of an orthopedic implant with multiple length sizes and compared the simulated results to experimental measurements obtained with the implant in the ASTM heating phantom. Furthermore, the electric field distribution, the SAR distribution, and the temperature rise for 16 different sizes of the implant, for two different implant orientations in the ASTM heating phantom, and for two typical MRI operating frequencies, 64-MHz (1.5-T) and 128-MHz (3-T), were evaluated.

MATERIALS AND METHODS

Numerical Modeling

The numerical modeling approach consists of four parts: 1) the development of the transmit RF coil; 2) the procedure to determine the best location (ie, worst-case) for the device placement in the ASTM heating phantom; 3) the electromagnetic and thermal simulations; and 4) the postprocessing of the data.

Two high-pass RF transmit body coils were used in the computational study. One represented a 64-MHz RF coil (1.5-T) and the second represented a 128-MHz RF coil (3-T). Rather than modeling the exact physical RF coil where capacitors, excitation sources, and metallic constructs all need to be modeled, the nonphysical coil uses electric currents enforced on the individual rungs. The tuning capacitors with different capacitance for 64-MHz and 128-MHz RF coil were only required to be placed inside the end rings to make sure the RF coil worked at the corresponding resonant frequency. To determine the capacitance value, several broadband simulations need to be performed to ensure the resonant frequency is either 64 MHz or 128 MHz for two different RF coils. For simplicity, the RF coil was modeled with eight rungs as developed in the SEMCAD-X manual (4). For all simulations the commercially available simulation package SEMCAD-X was used (4). Such simplification ignores the potential interaction between the implantable devices and the RF coil. However, such interaction is expected to be low due to the spacing between the RF coil and the implantable. In addition, the device is placed inside the gel phantom.

Once the RF coils were developed and their operating modes were verified (6,7), the location of the maximum electric field inside the ASTM heating phantom was determined (3). To evaluate the maximum electric field inside the ASTM phantom, the ASTM heating phantom was placed into each RF coil. The center of the "trunk" section of the ASTM phantom was placed at the center of the RF coil. The bottom of the phantom was 23.85 cm above the lowest point of the RF coil. With this phantom placement, electromagnetic simulations were performed to determine the electric field distributions within the ASTM heating phantom (8,9). From simulations, it was determined that the maximum electric field locations were about 2 cm away from the vertical side walls of the phantom close to the mid-axial plane. Thus, these locations were selected to place the implant to maximize the exposure and minimize the measurement uncertainty relative to MRI-related heating.

The orthopedic implant, the Basis Spinal System (Medtronic, Spinal and Biologics, Memphis, TN), used in this study consisted of a metallic plate and four screws as shown in Fig. 1. The length of this implant varies from 21–107 mm, depending on the length needed for the patient. The length of the four screws (15 mm) does not vary. To maximize the heating for this implant, it was placed in the ASTM phantom at the position determined previously to yield the worst-case heating (ie, close to the phantom wall). It should also be noted that the electric field can penetrate deeper into the ASTM phantom at the lower frequency. Therefore, for the purpose of testing, the implant was placed in a vertical mid-position, mid-torso position in the gelled-saline as shown in Fig. 1, as previously described (3).

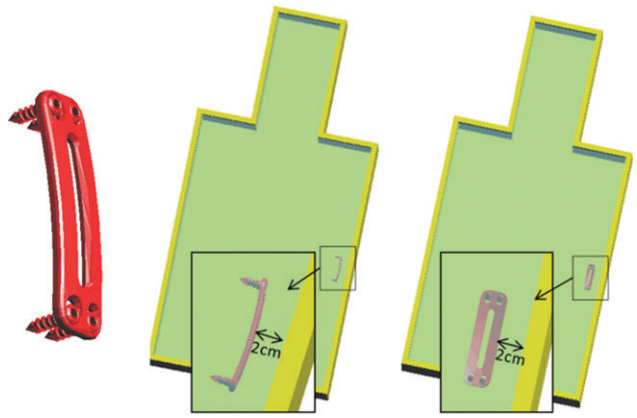

Figure 1. Illustration of the orthopedic implant and the placement of two different orientations: orientation 1 (middle) and orientation 2 (right) for the orthopedic implant in the ASTM heating phantom.

The next step was to place the implant of different sizes inside the ASTM phantom as shown in Fig. 1. The spacing between the device and the side wall was 2 cm for all simulations. Two orientations, screws perpendicular (middle picture in Fig. 1) and parallel (right picture in Fig. 1) to the vertical side walls were studied. In the first orientation (perpendicular), the screws of the device were pointing towards the center of the ASTM phantom while the second orientation (parallel) had the screws pointing towards the top surface of the phantom, which is the physiologically relevant orientation.

In this study the length of the RF coil rungs was 65 cm while the diameter of the top and bottom rings was 62.5 cm. The ASTM phantom consists of a plastic box with $\varepsilon_r = 3.7$ and $\sigma = 0$ S/m. The gelled-saline has a relative dielectric constant of $\varepsilon_r = 80.38$ and conductivity of $\sigma = 0.448$ S/m. In the numerical simulations, 16 different sizes of the orthopedic implant were used with lengths varying from 21 mm to 107 mm, as shown in Tables 1 and 2. The orthopedic implants with different lengths were modeled as perfect electric conductors. The mesh resolution for ASTM phantom is 2 cm, which applies to both the plastic box and the gelled-saline. For the orthopedic device, the resolution of finite difference time domain (FDTD) mesh was set to 1 mm to make sure the tip of the screw as well as the contour of the metallic plate were clearly modeled in numerical simulation. For all different implant lengths, the final grid sizes are between 10 million to 20 million cells. Simulations were accomplished using the aXware acceleration feature in SEMCAD-X with T C1060 graphic card which is able to handle the structure up to 90 million cells with a 30 times speed up compared with Intel Core i7-920 processor. To ensure the convergence of the electromagnetic simulations, the simulation time was set to 15 periods for both 1.5-T/64-MHz and 3-T/128-MHz simulations. The final results were normalized to a 2 W/kg whole-body SAR by integrating the total power loss inside the ASTM phantom and divided by the mass of the ASTM phantom. In this study, the power loss was evaluated in the gelled-saline (shell has zero conductivity) and the weight was also only evaluated on the gel for normalization.

The temperature increase in ASTM heating phantom is calculated using the heat transfer equation (10):

$$\rho c \frac{\partial T}{\partial t} = \nabla \cdot (k \nabla T) + \sigma |E|^2 \qquad [1]$$

The thermal conductivity for ASTM plastic box, ASTM gelled-saline, and the device are 0.2 W/m/K, 0.42 W/m/K, and 7 W/m/K, respectively. The specific heat capacitor for gelled-saline is 3200 J/kg/K. The specific heat capacitor for plastic box and device are not

Table 1
Maximum 1g Averaged SAR for the Orthopedic Implant at Different Lengths (1.5-T/64-MHz Transmit RF Coil) for a Whole Body Averaged SAR of 2 W/kg

Length of model (mm)	Peak 1g averaged SAR (W/kg)	
	Orientation 1	Orientation 2
Without implant	9.8	
21	15.8	15.8
23	15.8	17.1
25	17.1	18.3
27	18.3	19.5
30	20.7	20.7
32	22.0	23.2
37	25.6	26.8
41	29.3	29.3
43	30.5	30.5
45	31.7	31.7
47	34.2	33.0
50	34.2	37.8
62	47.6	48.8
67	47.6	50.0
87	67.1	70.8
107	84.2	91.5

Table 2
Maximum 1g Averaged SAR for the Orthopedic Implant at Different Lengths (3-T/128-MHz Transmit RF Coil) for a Whole Body Averaged SAR of 2 W/kg

Length of model (mm)	Peak 1g averaged SAR (W/kg)	
	Orientation 1	Orientation 2
Without implant	5.31	
21	8.6	8.6
23	8.6	8.6
25	8.6	10.6
27	10.6	10.6
30	12.4	12.4
32	12.4	14.2
37	15.9	15.9
41	17.7	17.7
43	17.7	19.5
45	19.5	21.2
47	21.2	21.2
50	23.0	24.8
62	31.9	31.9
67	31.9	33.6
87	40.7	42.5
107	42.5	42.5

important in the heat transfer simulation since only the temperature increase in ASTM gelled-saline was investigated. Initially, the baseline temperature of 19°C was set for the entire region. Thermal simulations were then conducted. Following a typical experimental procedure, for the initial 300 seconds the RF power was off. Then for the next 900 seconds (15 minutes) the RF power was turned on and followed by another 200 seconds off. This provides a complete transient behavior of the temperature rise near the implantable devices.

Experimental Testing

A 1.5-T/64-MHz MR system (Magnetom Siemens Medical Solutions, Malvern, PA) and 3-T/128-MHz MR system (Excite, General Electric Healthcare, Milwaukee, WI) were used for testing. The body RF coil was used to transmit RF energy in each case. Relatively high levels of RF power were used as reported by the MR system in each case and verified using calorimetry. The landmark position for each MRI procedure was at the center of the thorax as described in the modeling approach (thus, the center of the device) of the head/torso ASTM head/torso phantom, with multiple section locations obtained through the Basis Spinal System (67-mm length version, Medtronic, Memphis, TN), as previously described (1).

Temperature recordings were obtained in this experiment using a four-channel Model 3100 Fluoroptic Thermometry System (Lumasense, Santa Clara, CA) previously demonstrated to be MRI-compatible and unperturbed at static magnetic field strengths up to 9.0-T (ie, an MR spectrometer). This thermometry system has small fiber-optic probes (Model SFF-2; 0.5-mm diameter) that respond rapidly (response time, 0.25 sec; sensitive volume radius, less than 1 mm), with an accuracy and resolution of ±0.1°C. The thermometry system was calibrated immediately before obtaining temperature measurements for each experimental condition. The Basis Spinal System had thermometry probes attached to record representative temperatures, based on the simulation analysis.

Protocol

The gelled-saline-filled ASTM head/torso phantom was placed in the 1.5-T and then the 3-T MR system rooms, respectively, and allowed to equilibrate to these environmental conditions for more than 24 hours for each MRI-related heating test. The fan for each MR system was not on during each experiment. There was sufficient thermal equilibrium between the phantom and surrounding temperature such that the temperature of the phantom did not change by more than 0.1°C during the pre-MRI observation time for a period of 15 minutes for each MRI-related heating experiment.

Sufficient time was allowed to elapse between experiments (facilitated by thoroughly stirring and mixing the gelled saline) to permit the gelled-saline to return to thermo equilibrium. This was verified by recording temperatures in multiple positions in the gelled-saline-filled head/torso phantom prior to each heating test. The highest temperature changes recorded for the thermometry probes are reported herein for the orthopedic implant tested at 1.5-T/64-MHz and 3-T/128-MHz.

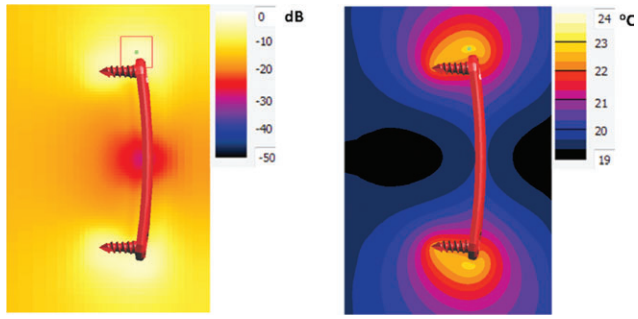

Figure 2. Log-scale representation 1g averaged SAR (left) and linear scale temperature (right) distributions near the orthopedic implant of 67 mm in length for a whole body averaged SAR of 2 W/kg.

RESULTS

Based on the numerical procedure described herein, a set of electromagnetic simulations was performed for both 1.5-T/64-MHz and 3-T/128-MHz transmit RF coil conditions. In all electromagnetic simulations the results were normalized to a whole body (or whole phantom) averaged SAR of 2 W/kg.

The 1g averaged SAR distribution for the 67 mm length Basis Spinal System is shown on the left side of Fig. 2. In addition to the SAR distributions, the temperature distribution near the device is also given on the right side of Fig. 2. The small green squares in the figures indicate the locations of maximum 1g averaged SARs and the temperature rises, respectively. As indicated in the figure, the 1g averaged SAR distribution and the temperature rise demonstrated a good correlation. However, in some simulations the maximum temperature rise location deviated from the location of the maximum 1g averaged. To accurately capture the maximum temperature rise, thermal simulations are required.

Table 1 shows the peak 1g averaged SAR for the orthopedic implant of different lengths for the 1.5-T/128-MHz system. For this implant, the SAR increases as its length increases. Based on the findings, the maximum heating locations are expected around either ends of the implant or the tips of the screws.

The SAR distribution within the ASTM phantom for the same implant was investigated at 3-T/128-MHz for all different possible lengths for this device. The results of this study are shown in Table 2. As the length of the implant increases, the local SAR enhancement due to the presence of the implant also increases. However, for this particular placement the SAR value at 1.5-T/64-MHz near the implant was higher than that at 3-T/128-MHz. This can be explained as the incident field strength on the implantable devices. Since 3T/128-MHz systems are

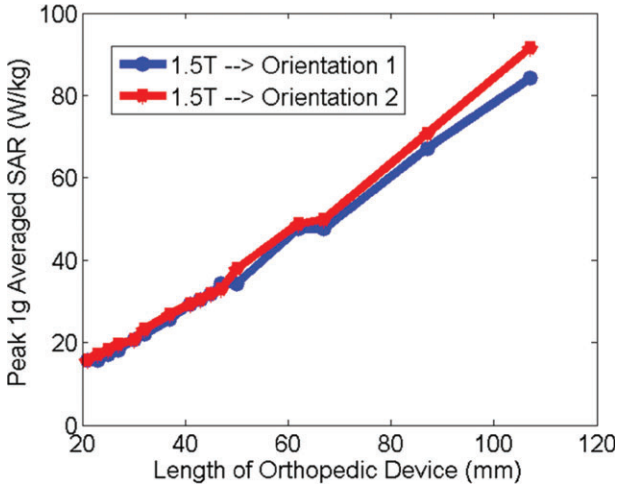

Figure 3. Peak 1g averaged SAR value as a function of orthopedic implant length for two different orientations at 1.5-T/64-MHz for a whole body averaged SAR of 2 W/kg.

operating at a higher frequency compared to 1.5-T/64-MHz scanners, more energy loss can be expected along the path from the surface of the ASTM phantom to the implant. Therefore, the incident electric field onto the implant at 3-T/128-MHz could be lower and, consequently, a lower induced heating near the tip of the same device at high frequency. In addition, we should point out that current studies place the device at the worst-case heating locations. If these devices are placed at the center of the ASTM phantom, due to the lower electric field at the center region, the temperature rise for the same implantable device should be lower.

In Figs. 3, 4, the peak 1g averaged SAR as a function of implant length at 1.5-T/64-MHz and 3-T/128-MHz are displayed. As indicated in the figures, peak 1g averaged SAR for both implant orientations are similar. They both increase as the implant length

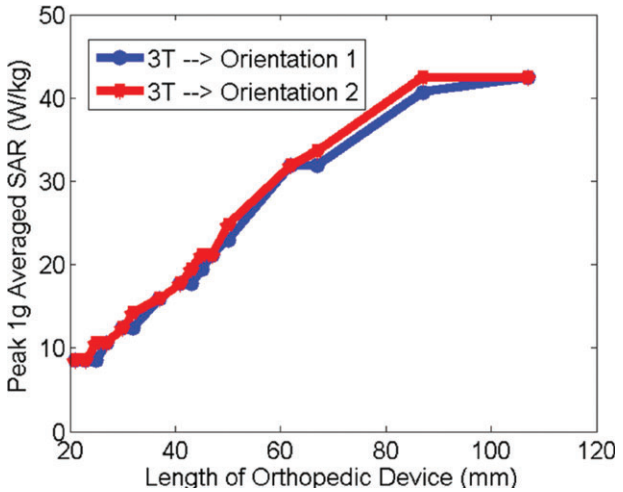

Figure 4. Peak 1g averaged SAR values as a function of orthopedic implant length for two different orientations at 3-T/128-MHz for a whole body averaged SAR of 2 W/kg.

increases. As shown in the figures, for the same level of input power at 3-T/128-MHz shows lower SAR near the "end" region, indicating possible lower heating for 3-T/128-MHz. Also indicated in Fig. 4 is that the SAR values for this device at 3-T/128-MHz seem to reach a plateau near 100 mm in implant length. This could be explained as the resonant wavelength effect (11). When the implant length is shorter than 100 mm, this length is less than half the wavelength at 3-T/128-MHz inside the gelled-saline, which is about 130 mm. For such scenarios, the maximum heating locations will probably be close to the ends of the implants. However, as the length increases, the implant's dimensions can become comparable to the wavelength of the incident electromagnetic field.

Due to the resonant effects as well as the phase variation of the incident field along the implant, the potential heating will no longer have the monotonic increment trend. Simulations were not performed beyond 107 mm because this particular implant is not available in lengths greater than 107 mm.

As mentioned above, the peak 1g averaged SAR location near the implanted device is a good indication where the maximum temperature rise may occur. To obtain the actual temperature rise, thermal simulations need to be carried out. This can be achieved by performing additional thermal simulations based on the bio-heat equation. To determine the temperature rise as a function of time, computational thermal sensors are placed near the locations on the implant where the maximum temperature rises are expected. All thermal simulations were performed with a whole-body averaged SAR of 2 W/kg.

Carefully designed temperature measurements were carried out for both 1.5-T/64-MHz and 3-T/128-MHz MR systems. As indicated in Fig. 5, the temperature probes were placed near the locations where

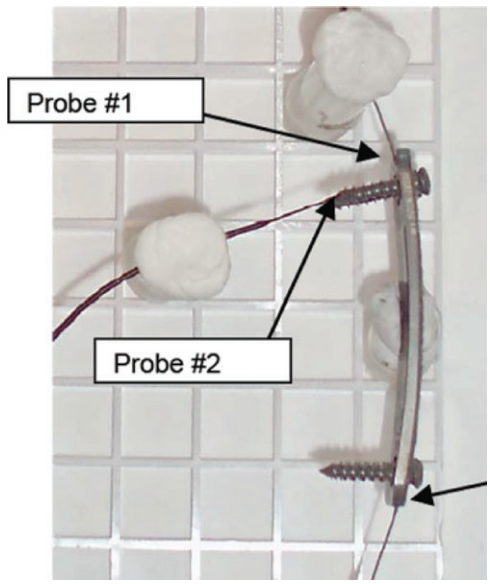

Figure 5. Positions for the fluoroptic thermometry probes, #1 and #2, relative to the orthopedic implant, Basis Spinal System. Black arrows indicate the tip locations for temperature probes.

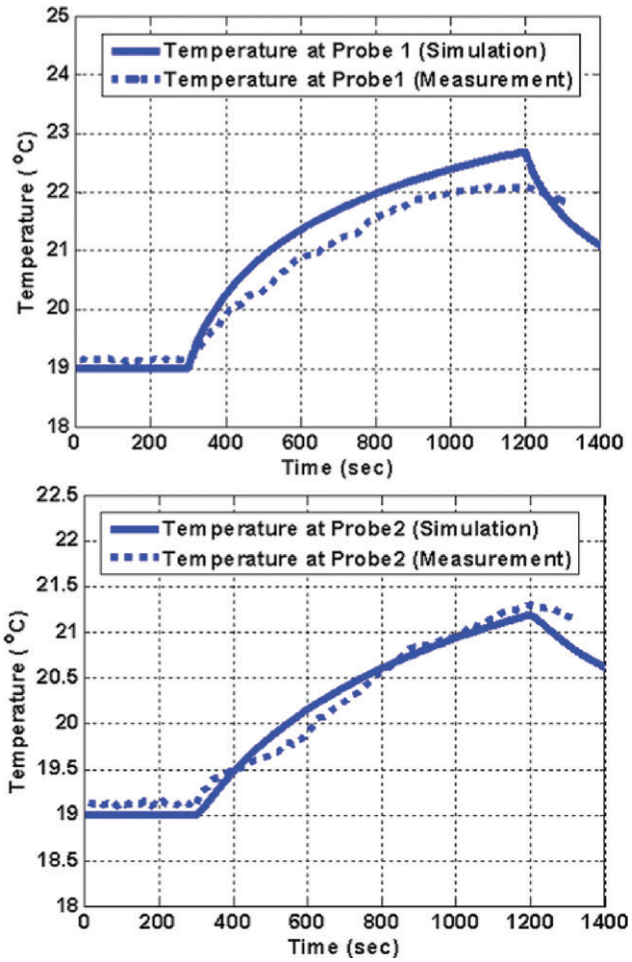

Figure 6. Simulated and measured temperature rises at temperature Probe 1 and Probe 2 for 1.5-T/64-MHz MRI system for a whole body averaged SAR of 2 W/kg.

maximum temperature rise was expected according to our simulation results. Figure 6 shows the simulated and measured temperature rise over time for 15 minutes at the two temperature probe locations as a function of time for 1.5-T/64-MHz conditions. As indicated in Fig. 6, the measurement and simulation results agree well with each other.

Similarly, the temperature simulations were performed for a 3-T/128-MHz MR system based on the SAR results obtained previously. Table 3 shows the temperature rise after 15 minutes for both 1.5-T/64-MHZ and 3-T/128-MHz at probe locations obtained by the simulations and measurements. As clearly indicated in the table, an acceptable correlation was observed.

DISCUSSION

From the electromagnetic and thermal simulation results, it can be clearly seen that numerical techniques were able to provide a good assessment of the maximum heating location for the evaluated orthopedic implant tested. For this particular orthopedic implant, the maximum heating locations were close to the tips of the screws and the ends of the implant. As the length of this orthopedic implant increases, especially when the device length is comparable to the wavelength of the MR operating frequencies, the heating patterns as well as the maximum heating location appear to be device-dependent.

From this study, the findings suggest that, when the orthopedic implant's length is less than 100 mm, the maximum heating of the device is almost linearly proportional to its length. This can be explained as a wavelength effect. At 1.5-T/64-MHz, the electromagnetic incident wavelength is ~4.5 m in free space and ~0.52 m in the gelled-saline. When this orthopedic implant's length is less than 100 mm, the overall length is still less than a quarter wavelength. Therefore, it is not expected for the incident field to have a large phase variation or have resonant effect. However, for 3-T/128-MHz electromagnetic signals, the wavelength in gelled-saline is 0.26 m. The device length of 100 mm is approaching the half-wavelength resonant dimension. Therefore, the incident field will have a large phase variation along the device and the device will exhibit resonant behavior. Thus, a monotonic relation between the maximum heating and the device length will no longer be valid. For device lengths over 100 mm, an electromagnetic/thermal simulation is recommended to be performed at centimeter increments to capture the maximum heating for different lengths.

This investigation demonstrated that with numerical calculations it is possible to quickly predict which device configuration and size will lead to maximum heating as well as the maximum heating location for the device. With this information, one can correctly place the temperature probes for actual measurements. This method can significantly reduce the uncertainty of the temperature probe placement, as well as the number of devices that need to be tested. Consequently, it can significantly reduce the time and expense of testing performed to evaluate MRI-related heating. Using this testing procedure, one can quickly predict the worst-case heating of a device family.

In conclusion, electromagnetic and thermal simulations were used to determine the worst-case heating for an orthopedic implant with lengths from 21–107

Table 3
Simulated and Measured Temperature Changes for 67 mm Length Implant in 1.5-T/64-MHz and 3-T/128-MHz MR Systems After 15 Minutes of RF Exposure at the Two Temperature Probe Locations for a Whole Body Averaged SAR of 2 W/kg

	1.5-T/64-MHz simulation	1.5-T/64-MHz measurement	3-T/128-MHz simulation	3-T/128-MHz measurement
Probe 1	3.6°C	3.1°C	2.1°C	1.9°C
Probe 2	2.2°C	2.2°C	1.6°C	1.7°C

mm. For this particular implant family, it was observed that the temperature rise is related to the length of the implant and the maximum temperature rise locations are close to the ends of the implant or at the screw tip. MRI-related heating experiments were performed to record temperatures to validate the simulation results and good correlations were observed. The findings demonstrated that electromagnetic and thermal simulations may be used as an excellent tool to provide the heating pattern for implants and to identify the maximum heating locations for the entire device family. If only a measurement technique is used, temperature probes need to be placed near the entire device to determine the worst-case heating spot near the device. Therefore, numerical modeling is an accurate and efficient way to determine the worst-case heating.

Because the maximum heating can change for different implant sizes or configurations, the location of the maximum heating is important for a proper measurement setup. Numerical simulations provide the means to drastically reduce the number of measurements needed to assess the worst-case configuration and size for an entire device family. The numerical results are also the only practical way to find the location of the maximum heating on the implant surface and to place the temperature probe at this position during the measurements. Importantly, for validation purposes, the numerical simulations should always be accompanied by proper temperature measurements.

REFERENCES

1. Shellock FG. Reference manual for magnetic resonance safety, implants and devices: 2012 edition. Los Angeles: Biomedical Research Publishing; 2012.
2. Woods TO. Standards for medical devices in MRI: present and future. J Magn Reson Imaging 2007;26:1186–1189.
3. ASTM. Standard F2182-11a, 2011, standard test method for measurement of radio frequency induced heating on or near passive implants during magnetic resonance imaging. West Conshohocken, PA: ASTM International, 2011, DOI: 10.1520/F2182–11A, www.astm.org
4. SEMCAD X. Reference manual for the SEMCAD simulation platform for electromagnetic compatibility, antenna design and dosimetry. SPEAG – Schmid & Partner Engineering.
5. Neufeld E, Kuhn S, Szekely G, Kuster N. Measurement, simulation, and uncertainty during MRI. Phys Med Biol 2009;54: 4151–4169.
6. Chen J, Feng Z, Jin JM. Numerical simulation of SAR and B1-field inhomogeneity of shielded RF coils loaded with the human head. IEEE Trans Biomed Eng 1998;45:650–659.
7. Jin J. Electromagnetic analysis and design in magnetic resonance imaging. Boca Raton, FL: CRC Press; 1998.
8. Angelone LM, Ahveninen J, Belliveau JW, Bonmassar G. Analysis of the role of lead resistivity in specific absorption rate for deep brain stimulator leads at 3T MRI. IEEE Trans Med Imaging 2010; 29:1029–1038.
9. Powell J, Papadaki A, Hand J, Hart A, McRobbie D. Numerical simulation of SAR induced around Co-Cr-Mo hip prostheses in situ exposed to RF fields associated with 1.5- and 3-T MRI body coils. Magn Reson Med 2011 [Epub ahead of print].
10. Oh S, Webb AG, Neuberger T, Park B, Collins CM. Experimental and numerical assessment of MRI-induced temperature change and SAR distributions in phantoms and in vivo. Magn Reson Med 2010;63:218–223.
11. Mattei E, Triventi M, Calcagnini G, et al. Complexity of MRI induced heating on metallic leads: experimental measurements of 374 configurations. Biomed Eng Online 2008;7:11.